Research Square

Preprints are preliminary reports that have not undergone peer review.
They should not be considered conclusive, used to inform clinical practice,
or referenced by the media as validated information.

Ultra-Stable Weyl Topology Driven by Magnetic Textures in the Shandite Compound Co3Sn2S(2−x)Se(x)

Dang Khoa Le

kdl222@usf.edu

University of South Florida

Dang Khoa Le

kdl222@usf.edu

University of South Florida

Article

Keywords: spin-chiral interaction, magnetic interactions, Weyl topology, phase transition

Posted Date: April 23rd, 2026

DOI: https://doi.org/10.21203/rs.3.rs-9315959/v1

License: This work is licensed under a Creative Commons Attribution 4.0 International License.
Read Full License

Additional Declarations: There is **NO** Competing Interest.

Version of Record: A version of this preprint was published at Communications Physics on November 18th, 2026. See the published version at https://doi.org/10.1038/s42005-026-02863-6.

Ultra-Stable Weyl Topology Driven by Magnetic Textures in the Shandite Compound $Co_3Sn_2S_{(2-x)}Se_{(x)}$

Dang Khoa Le[1*], Eklavya Thareja[1*], Bektur Konushbaev[1], Gina Pantano[1], Tom Saunderson[2,3], Manh-Huong Phan[1,4], Yuriy Mokrousov[2,5], Jacob Gayles[1†]

[1]Department of Physics, University of South Florida, Tampa, 33620, USA.
[2]Peter Grünberg Institut and Institute for Advanced Simulation, Forschungszentrum Jülich and JARA, 52425, Jülich, Germany.
[3]Institut für Physik and Halle-Berlin-Regensburg Cluster of Excellence CCE, Martin-Luther-Universität Halle-Wittenberg, D-06099 Halle (Saale), Germany.
[4]Center for Materials Innovation and Technology, VinUniversity, Hanoi, 100000, Vietnam.
[5]Institute of Physics, Johannes Gutenberg University Mainz, 55099, Mainz, Germany.

*Corresponding author(s). E-mail(s): kdl222@usf.edu; ethareja@usf.edu;
Contributing authors: kb3@usf.edu; gmpantano@usf.edu; tsaunder@uni-mainz.de; huong.pm@vinuni.edu.vn; phanm@usf.edu; y.mokrousov@fz-juelich.de; gayles@usf.edu;
†These authors contributed equally to this work.

Abstract

The shandite compounds garnered great interest due to exhibiting complex magnetic interactions and Weyl fermions. While previous results have shown magnetic transport phenomena driven by topological features, there is little understanding of magnetic interactions and their effect on Weyl features. Here, we employ first-principles calculations to investigate such compounds, including $Co_3Sn_2S_2$, Co_3Sn_2SeS, and $Co_3Sn_2Se_2$. The Dzyaloshinskii-Moriya interaction (DMI) is found to be negligible even when inversion symmetry is broken, while exchange interaction and magnetocrystalline anisotropy are present. However, we identify that a decisive role will be played by spin-chiral interaction

(SCI) arising from the kagome lattice topology in stabilizing magnetic textures. Furthermore, we demonstrate that short-wavelength magnetic textures drive phase transitions in the Weyl nodes, leading to band flattening and gap opening. This newly identified SCI, together with the associated electronically driven phase transitions, provides a promising route for manipulating transport properties in spintronic devices.

Keywords: spin-chiral interaction, magnetic interactions, Weyl topology, phase transition

1 Introduction

The cornerstone of modern electronics rests on the ability to switch conductivity states through external fields, such as n-p junctions and gate transistors, or by altering spin alignment, as seen in giant magnetoresistance devices. Modern devices demand a deeper understanding of how to realize high mobility and controllable coupling between electronic and magnetic structures. Topological materials, via spin-momentum-locked bands, require the lack of time reversal or inversion symmetry and pave a way for paradigm shifts in electronic and magnetic phenomena [1, 2]. Topological materials, including Dirac, Weyl (magnetic and nonmagnetic), and nodal-line semimetals, exhibit remarkable features resulting in large Berry curvature effects, the imaginary part of the quantum geometry, such as the Anomalous Hall effect (AHE), suppressed backscattering, and high carrier mobilities [2, 3, 4]. Despite these advances, systematic manipulation of Dirac and Weyl crossings has so far been achieved primarily in Moiré bilayer graphene [5, 6, 7] and charge-density-wave systems [8, 9]. In magnetic systems, the interplay of Berry curvatures defined in distinct geometric spaces hinders progress, as it is not yet well understood [10, 11]. The antisymmetric Dzyaloshinskii–Moriya interaction (DMI) [12, 13], which requires broken inversion symmetry and is closely tied to phase-space Berry curvature [14], appears to be incompatible with magnetic Weyl semimetals, which typically preserve inversion symmetry in the momentum space Berry curvature.

Nominally, the DMI is the crucial chiral ingredient required to stabilize real-space topological spin textures such as skyrmions [15, 16], which have attracted strong interest for potential applications in racetrack memory devices [17, 18]. The primary electrical signature of skyrmions and their size is the topological Hall effect [19]; however, in multi-band metals, this contribution is typically minimal compared to the anomalous and ordinary Hall effects [20]. In the simplest picture, the size of magnetic textures is determined by competing energy scales, where domain wall widths are set by the ratio of exchange to the square root of magnetocrystalline anisotropic energy, while skyrmion sizes scale with the ratio of DMI to exchange [21, 22]. Stabilizing compact magnetic textures requires either a large DMI or strong anisotropy terms that scale quadratically and linearly with spin-orbit coupling, respectively [21, 23]. The DMI is both large and anisotropic, which can dramatically alter the spin-momentum locking in topological materials and diminish their mobility. However, in the presence of frustrated magnetic lattices, especially kagome lattice symmetry, a novel spin-chiral interaction (SCI) emerges—which is intrinsically maximized by the local geometry [24, 25, 26, 27]. The SCI can stabilize magnetic textures [24] without sacrificing the Weyl topology and other novel transport phenomena[4].

Such a case is realized in the layered shandite compound $Co_3Sn_2S_2$ and its stoichiometric variants $Co_3Sn_2S_{(2-x)}Se_{(x)}$, which crystallize in the rhombohedral space group $R\bar{3}m$ (No.166). The magnetic Co atoms form a kagome network interlaced with Sn and S/Se atoms, with inversion symmetry preserved for $x = 0, 2$ but broken for $x = 1$ (see Fig. 1 a). The symmetry allows for anti-aligned DMI [28] vectors on parallel kagome planes of Co atoms that globally sum to zero for $x = 0, 2$ and should nominally be finite for $x = 1$, which lacks inversion symmetry. $Co_3Sn_2S_2$ was among the first predicted and experimentally confirmed magnetic Weyl semimetal, exhibiting an anomalous Hall conductivity ($\sigma_H^A = 1130$ $\Omega^{-1}\ cm^{-1}$) close to the maximum value for a two-band system [29, 30]. Together with their Se-substituted counterparts, these compounds display Curie temperatures ranging from 150 K to 180 K [31, 32] that decrease with increasing Se concentration. However, the precise magnetic ground state of $Co_3Sn_2S_{(2-x)}Se_{(x)}$ remains inconclusive. Furthermore, the microscopic origins of the in-plane magnetic stabilization and anisotropy remain controversial [33, 34]. Reports include magnetic susceptibility measurements indicating an A-phase pocket reminiscent of skyrmion-hosting systems [35, 36], and large conductivity changes in the presence of domain wall networks [37, 38, 39], and quasi-flatbands associated with the magnon mode population [40, 41, 42]. In this work, we resolve the outstanding questions related to the competing exchange terms and demonstrate how spin-chiral interaction (SCI) and different magnetic interactions influence the exotic, topology-driven bands that emerge in this shandite family.

We use first-principles calculations to investigate the magnetic structure and its influence on the topological electronic structure in the magnetic Weyl semimetals $Co_3Sn_2S_{(2-x)}Se_{(x)}$ for $x = 0, 1, 2$. We evaluate the SCI and DMI fields for all systems and observe that even in the inversion-asymmetric case ($x = 1$), the SCI is significantly larger than the DMI. In all cases of the SCI calculations with noncoplanar spin configuration, the Weyl nodes persist. For high symmetry propagating spin-spirals, the nodes transition from Type-I Weyl to Type-II Weyl, and finally to a gapped state, as the wavelength is reduced to short periods. The Weyl nodes in the inversion-asymmetric compound Co_3Sn_2SSe ($x = 1$) show the strongest stability against magnetic textures. We further calculate the exchange stiffness using homogeneous spin spirals, i.e., frozen magnons, along the major crystallographic axes, obtaining values that qualitatively agree with and follow the trends of previous experimental reports of the Curie temperature [31, 32]. Our calculations of the magnetocrystalline anisotropy (MCA) reveal a systematic increase with enhanced spin-orbit interaction from $x = 0$ to $x = 2$.

2 Results

2.1 Spin-Chiral Interactions in Stacked Kagome Lattice

A noncoplanar arrangement of spin moments with maximal scalar chirality product $\chi_{ijk} = \vec{S}_i \cdot (\vec{S}_j \times \vec{S}_k)$ is shown in Fig.1. a, which results in nonzero SCI. Fig.1. b shows the evolution of the projected density of states (DOS) from a conventional ferromagnetic Weyl and noncoplanar Weyl to a gapped noncollinear spin-spiral state. The angle θ (inset of Fig.1. a) describes the change of spin-configuration of each magnetic Co atom in noncoplanar configurations. We calculated the exchange energy of $Co_3Sn_2S_{(2-x)}Se_{(x)}$ by considering the dependence of energy dispersion on the angle θ without spin-orbit coupling (SOC). $Co_3Sn_2S_2$ exhibits the largest exchange energy, while $Co_3Sn_2Se_2$ shows the weakest. The

intra-cell energy dispersion of our shandite family depends on three magnetic interactions, the DMI, magnetocrystalline anisotropy (MAE), and the spin-chiral interaction (SCI) when the SOC effect are considered. We obtained the energy functions as $E_{DMI} \sim \sin(\theta)$ (orange dashed lines), $E_{MAE} \sim \sin^2(\theta)$ (green dash-dot lines) and $E_{SCI} \sim \sin^3(\theta)$ (blue broken lines) by using Eq. 4 based on the spin configurations in Eq.1. We evaluated the contribution of these interactions based on first, second, and third order correction terms to the exchange energy. The total DMI in the out-of-plane direction is zero in comparison to the SCI, except for the inversion lacking Co_3Sn_2SeS. The strength of SCI is 0.78 meV, 0.86 meV, and 0.87 meV for $x = 0, 1$ and 2, respectively, and in correspondence with the increase in SOC strength. While this show the SCI dominates the intracell spin-orbit interactions, one must also consider intercell interactions for the stabilization of magnetic textures.

2.2 Magnetic Energy Scales Underpinning Noncollinear Textures

We calculated the spin exchange stiffness (A) and magnetocrystalline anisotropy (K_i) of the shandite compounds. The exchange energy was calculated for two spin configurations, the homogeneous spin spiral and noncoplanar magnetic texture. The energies for our spin-spiral calculations were computed without SOC as flat spin spirals with a cone angle $\theta_i = \pi/2$. Fig. 2(a-c) shows the energy dispersions for the spin spirals along the $q = [1, 0, 0]$ (red-circles), $q = [1, 1, 0]$ (blue-triangles) and the $q = [1, 1, 1]$ (green-squares) directions in the three $Co_3Sn_2S_{(2-x)}Se_{(x)}$ compounds. A is fitted to the energy dispersion of the spin spiral by the simplified version of $E(q) = A|\mathbf{q}|^2$ [43]. Table 1 shows the calculated spin stiffness exchange for the noncoplanar 2Q and spin spiral magnetic textures. The largest A for all compounds is along the $[1, 1, 0]$ direction, where A decreases from 450.88 meV for $Co_3Sn_2S_2$ ($x = 0$) to 332.25 meV for Co_3Sn_2SeS ($x = 1$) and 264.07 meV for $Co_3Sn_2Se_2$ ($x = 2$). The Curie temperature was calculated from the spin exchange stiffness from $A = C^{2/3}kT_c$, where C is determined by intrinsic magnetic variables, including critical exponent β and magnetization at absolute temperature $0K$ [44]. The Curie temperature of $Co_3Sn_2S_2$ is 173K, in good agreement with the experimental value of 169K. When the Se/S ratio increases, the Curie temperature decreases due to a decrease in spin-exchange stiffness and in line with experimental trend [31, 32].

The stabilization of the magnetic structure is also determined by the magnetic anisotropy, which indicates the preferred alignment of the magnetic sites. The magnetic anisotropic energy of $Co_3Sn_2S_{(2-x)}Se_{(x)}$ is calculated in collinear magnetic textures with the presence of SOC. We plot the magnetic anisotropy energy surface of the $Co_3Sn_2S_2$, Co_3Sn_2SeS, and $Co_3Sn_2Se_2$ in Fig.2(d-f). The MCA constants, K_i, are fitted to the energy surface by the symmetry of the crystal surface [45]. Fig.2(d-f) illustrates a perpendicular magnetic anisotropy for all compounds, where the MCA energies along the z-direction are the lowest when the magnetic spin prefers to point out of the Kagome lattice. These results are consistent with those observed experimentally [46]. Among the three compounds, $Co_3Sn_2Se_2$ exhibits the highest MCA energy (1.2 meV), likely due to the large spin-orbit coupling of the Se atom compared to that of the S counterpart. This result is also consistent with the differences in the energy landscapes of the three systems shown in Fig.2(d–f). Using the obtained spin exchange stiffness and anisotropy energy, the domain wall width can be estimated from the relation $\delta_{DW} \simeq \pi\sqrt{A_{ex}/K}$. The calculated domain wall width of the $Co_3Sn_2S_2$ shandite compound is $\delta_{DW} = 3.47$ nm, whereas experimental measurements report $\delta_{DW} \sim 2$ nm [47, 48]. This

discrepancy likely reflects the influence of complex magnetic interactions, including spin-chiral interactions. The presence of such an interaction in shandite systems can further reduce the domain wall width, promoting the stabilization of noncollinear magnetic textures.

Table 1 Computed exchange and magnetic anisotropic interactions for the propagation directions of the q vector in $Co_3Sn_2S_{(2-x)}Se_{(x)}$.

Exchange stiffness	$Co_3Sn_2S_2$	Co_3Sn_2SeS	$Co_3Sn_2Se_2$
$A_{[1,0,0]}\ (meV)$	339.08	299.00	270.92
$A_{[1,1,0]}\ (meV)$	450.88	332.25	264.07
$A_{[1,1,1]}\ (meV)$	284.50	277.24	151.20
$A_{SC}\ \ (meV)$	210.53	186.74	174.08
Anisotropic energy	$Co_3Sn_2S_2$	Co_3Sn_2SeS	$Co_3Sn_2Se_2$
$K_0\ (meV)$	0.59	0.82	1.19
$K_1\ (meV)$	-0.60	-0.83	-1.20
$K_2\ (meV)$	0.003	0.002	0.001
$K_3\ (meV)$	0.001	-0.001	-0.023
Spin-chiral	$Co_3Sn_2S_2$	Co_3Sn_2SeS	$Co_3Sn_2Se_2$
$SCI\ (meV)$	0.78	0.86	0.87
DMI	$Co_3Sn_2S_2$	Co_3Sn_2SeS	$Co_3Sn_2Se_2$
$D\ (meV)$	0.000	-0.063	0.000

2.3 Spin spriral driven Weyl Phase Transitions

Magnetic textures, such as domain walls, significantly modify the Weyl electronic band structure in $Co_3Sn_2S_{(2-x)}Se_{(x)}$ compounds. In Fig. 3(a,c,e), we show how varying the length of homogeneous flat spin spirals ($\theta_i = \pi/2$) alters the band structure near Weyl crossings in $Co_3Sn_2S_2$. In the ferromagnetic state, $Co_3Sn_2S_{2-x}Se_{(x)}$ hosts magnetic Weyl cones near the high-symmetry L point (where L $= [1/2; 0; 0]$). It is worth mentioning that these topological features do not appear along the high-symmetry k path. Therefore, we select a specific k-path that intersects the Weyl nodes. The positions in k-space of the Weyl nodes in the ferromagnetic ground state are $W_{S_2} = [0.313; -0.056; -0.056]$, $W_{SeS} = [0.284; -0.085; -0.085]$, and $W_{Se_2} = [0.276; -0.102; -0.102]$. Here, the coordinates of the above k-points are in the fraction coordinates of the first Brillouin zone. Applying rotational symmetry C_{3z} yields similar Weyl nodes as reported in [49]. In Fig. 3(a), Type-I Weyl crossings are indicated in the red box for small spin spiral angles ($\phi \leq 45$) in $Co_3Sn_2S_2$. These features originate from the absence of time-reversal symmetry in $Co_3Sn_2S_2$ and $Co_3Sn_2Se_2$. With the variation of ϕ values, i.e. $\phi = 72°$, the Weyl nodes of these shandite compounds undergo a transition from Type-I Weyl to Type-II Weyl, highlighted in the blue box in Fig.3(c). When ϕ surpasses $90°$, these Weyl nodes become gapped as seen in the green box of Fig.3(e). The behavior of Weyl crossings in the band structures is presented in Supplementary Figure 1. However, due to inversion symmetry breaking arising from the substitution of S with Se atoms, we observe the magnetic Weyl nodes persist in Co_3Sn_2SeS even with $\phi \geq 90°$. In particular, the electronic bands exhibit double crossings along the chosen LA and LA$'$ k-path. Further investigations are necessary to understand the nature of these emergence crossings in Co_3Sn_2SeS compounds. Shandite systems undergo a sequence of topological phase transitions first, from

Type-I to Type-II Weyl semimetals (characterized as a second-order transition), and finally to a gapped state (characterized as a first-order transition). Under the noncollinear spin orientation, the existence of Weyl crossings in the band structures originates from the vertical mirror symmetry σ_v, while rotational symmetry C_{3z} preserves magnetic Weyl points with opposite Chern numbers $+1$ and -1 in the presence of SOC [49].

The topological phase transitions are also reflected in the density of states (DOS) shown in Fig.3 (b,d,f). We show the total DOS of $Co_3Sn_2S_2$ and the DOS in the regions where the Weyl points are located. A box of k-mesh is constructed around the k-path AA$'$ to demonstrate the variation of the DOS, as shown by the corresponding colors as in band structures in Fig. 3(b,d,f). We also projected DOS along the x-direction, where the left panel DOS corresponds to a positive projection, and the right panel DOS corresponds to a negative projection. As shown in Fig.3.(b) for $\phi \leq 36°$, the majority spin dominates the DOS near the Fermi energy, which is the positive region for spin-projected along the x direction $\langle S_x \rangle$. However, when ϕ increases, there is a redistribution from positive $\langle S_x \rangle$ to negative $\langle S_x \rangle$. It is apparent in Fig.3(d) there is an appearance of the DOS peaks near Fermi energy in the negative regions. The linear behavior appeared in the electronic states from the boxed DOS curve when the Weyl crossings gapped ($\phi \geq 90°$). Supplementary Figure 2 in Supplementary Information (SI) shows the band corresponding to the above DOS and reflects the gapped signature of the Weyl crossings. However, the behavior of DOS along the noted box that contains Weyl nodes does not affect the overall DOS of the systems. Since the Weyl cones only exist along a specific path (AA$'$) that passes through the high symmetry point L in the first Brillouin zone, not along the whole Brillouin zone. As the angle ϕ changes, the overall band structure of the shandite system alters drastically, while the magnetic Weyl crossings undergo a steady topological phase transition from type-I to type-II Weyl and eventually gapped as shown in Fig.3. Similar behavior can be found in $Co_3Sn_2Se_2$. Nevertheless, the magnetic Weyl nodes in Co_3Sn_2SeS still persist even with $\phi \geq 90°$ and form double crossings in the electronic band structure, leading to the nonzero DOS around the regions of the nodes.

2.4 Persistence of Weyl Geometry beyond Ferromagnetism

To obtain a thorough understanding of the evolution of homogeneous spin spiral to Weyl cones along in both momentum space and its energy in the electronic band structures, Fig.4 displays the positions of these magnetic Weyl points in momentum space and their energy according to the Fermi energy. While Fig. 4(a) and (b) illustrate the separation between the two Weyl nodes in the shandite system, Fig. 4(c) and (d) show the positions of the Weyl crossings relative to the Fermi energy for all three compounds. We also indicate Type-I to Type-II and gapped regions in red-, blue-, and green-colored regions to demonstrate the topological phase transition mentioned in the previous section.

Under the noncollinear spin spiral, for $Co_3Sn_2S_2$ and $Co_3Sn_2Se_2$, the distance of Weyl-points increases slightly as systems transform from Type-I (red regions) to Type-II Weyls (blue regions), as shown in Fig.4(a). During this process, we observed a downward shift of the Weyl crossing energies with respect to the Fermi energy, which is evident in Fig. 4(c). In addition, for Co_3Sn_2SeS, the Weyl-point distance increases, reaching nearly twice that of the ferromagnetic state. On the other hand, both Weyl cones of $Co_3Sn_2S_2$ and $Co_3Sn_2Se_2$ are gapped (indicated in the green region) as the spin spiral angle $\phi \geq 90°$. When increasing ϕ even further, these Weyl crossings persist in a gapped state with $x = 0, 2$

in $Co_3Sn_2S_{(2-x)}Se_{(x)}$. However, for Co_3Sn_2SeS, the Weyl nodes persist as a function of the angle ϕ. For the spin spiral direction $q = [1, 1, 1]$, we observe similar topological phase transitions, progressing from Type-I Weyl to Type-II Weyl, and ultimately to a gapped state. Nevertheless, the Weyl topological phase does not persist in the $q = [1, 1, 0]$ case, where the Weyl crossings become gapped with only a small change of spin spiral angle $\phi \geq 45°$. These results are available in Supplementary Figure 3. For the noncoplanar case shown in Fig.4(b,d), we found that minor variations in the separation of Weyl-crossings among the three systems, along with the shifts in their energy positions with varying angle θ. This indicates that the Weyl topology remains Type-I Weyl semimetal of all three compounds during the noncoplanar spin configurations.

3 Discussions

In absolute SCI strength, B20 compounds [24] indicate that MnGe (where $\chi^{SC}\kappa^{TO} = -3.17$ meV) surpasses $Co_3Sn_2S_{(2-x)}Se_x$. However, to compare these systems more meaningfully, we instead evaluate the differences in SCI values over magnetic moment by considering B_{eff}, the internal effective field, generated by noncoplanar spin configurations. For the B20 compounds, with a Mn magnetic moment of $1.96\mu_B$, B_{eff} is -1.61 meV$/\mu_B$, while for FeGe, which has a Fe moment of $0.78\mu_B$, B_{eff} is 0.27 meV$/\mu_B$. Surprisingly, for $Co_3Sn_2S_{(2-x)}Se_x$, even with a small magnetic moment of $0.356\mu_B$, B_{eff} values are 2.19 meV$/\mu_B$, 2.42 meV$/\mu_B$, and 2.44 meV$/\mu_B$ for $x = 0$, $x = 1$, and $x = 2$, respectively. These values demonstrate that the B_{eff} in $Co_3Sn_2S_{(2-x)}Se_x$ are of the same order of magnitude and larger than those in B20 compounds. Furthermore, the calculated SCI values are non-zero, while the DMI values vanis1h in our system. This distinction arises because the Kagome net's geometric nature persists across all $Co_3Sn_2S_{(2-x)}Se_x$ compounds. By contrast, DMI, which arises from the lack of inversion symmetry, vanishes at both $x = 0$ and $x = 2$. Co_3Sn_2SeS, the substitution of S with Se atoms introduces intrinsic inversion symmetry breaking, leading to a nonzero DMI—though this value remains smaller than the SCI, as noted previously. Notably, while the emergence of SCI in MnGe has been proposed to give rise to novel real-space spin textures [24] and can be measurable experimentally through the emergence of chiral magnetism [50, 51]. This suggests a similar mechanism to explain the observed phenomena in shandite compounds [46, 36]. In our system, the high B_{eff}, combined with the absence of other complicated spin-orbit terms, likely drives complex magnetic textures and enhances Weyl state stability. On the other hand, for MnGe, its chiral structure allows coexistence of complex spin-orbit terms, including DMI, biquadratic, cubic, and uncubic anisotropic interactions. However, these interactions are small compared to the SCI in $Co_3Sn_2S_{(2-x)}Se_x$.

As we investigate the behavior Weyl nodes with the effect of SCI, $Co_3Sn_2S_{2-x}Se_{(x)}$ displays the Type-I Weyl topology. This highlights that the Weyl topology exhibits high stability under noncoplanar spin configurations. The tunability of Weyl nodes through control of the spin spiral angle directly influences the electronic and accompanying transport properties of the shandite materials. The Berry curvature is determined not only by the Weyl-node separation but also by the specific type of Weyl node, including type-I, and tilted type-II, as reflected in the band structures. In all compounds considered, the momentum-space Weyl spin texture makes a negligible contribution to the DMI energy, indicating the absence of

phase-space geometric terms. The variation of the spin spiral angle drives a phase transition from type-I to type-II Weyl. The emergence of Berry curvature near the Fermi surface is expected to manifest experimentally as an increase in magnetoconductivity, arising from the broken time-reversal symmetry associated with the tilted Weyl spectrum. The presence of tilted and type-II Weyl nodes can enhance conductivity, especially hall conductivity in the shandite systems [52, 53, 54]. When the Weyl crossings evolve from type-II to a gapped state, magnetoconductivity decreases, which is anticipated, consistent with previous experimental observations [55, 56, 57]. This behavior is attributed to the Berry curvature, which modifies these observables during the topological transition from Weyl nodes to a gapped state. Our results provide a promising pathway for controlling topological Weyl crossings and their impact on the magnetic properties of the shandite systems.

In conclusion, we have shown that $\mathbf{Co_3Sn_2S_{(2-x)}Se_{(x)}}$ compounds exhibit significant spin-chiral interaction due to the underlying Kagome net, indicating that stabilizing non-collinear textures requires interactions beyond the Dzyaloshinskii–Moriya mechanism. We calculated the exchange stiffness for all three compounds, and the results agree with Curie temperature data. In these systems, Weyl nodes undergo a topological transition as the magnetic configuration is controlled, while Weyl crossings remain unchanged in non-coplanar textures. Magnetic Weyl cones near the Fermi energy can be modified, confirming phase transitions from Type-I to Type-II and eventually to a gapped state. Further investigation of quantum-geometric tensors in Kagome systems is needed to explore these transitions. Our work on the connections of spin structures and Weyl manipulation lays the foundation for understanding nontrivial features in similar Kagome systems, thereby enabling systematic engineering of magnetic properties for advanced spintronics.

4 Methods

4.1 DFT+ Generalized Bloch Theorem

To investigate how magnetic textures affect the topological band structure of $\mathbf{Co_3Sn_2S_{(2-x)}Se_{(x)}}$, as shown in Fig.1.a, we use the full-potential linearized augmented plane wave (FLAPW) method in the FLEUR code [58, 59]. We employ Perdew-Burke-Ernzerhof exchange functionals [60] for approximating exchange-correlation energy. For all three materials, the plane-wave cutoff is $4.0a.u^{-1}$. The k-point mesh is $26 \times 26 \times 26$ for all compounds. These criteria ensure self-consistent calculations for coplanar, noncoplanar, and magnetic anisotropy cases.

Our shandite compounds are in bulk form and have a rhombohedral crystal structure. The muffin tin radii are 2.28 Bohr for Co, 2.75 Bohr for Sn, 1.78 Bohr for S, and 1.95 Bohr for Se. The lattice parameters are as follows $\mathbf{Co_3Sn_2S_2}$ has $a = 5.3747$ Å and $\alpha = 59.964°$; $\mathbf{Co_3Sn_2SeS}$ has $a = 5.47483$ Å and $\alpha = 59.13°$; $\mathbf{Co_3Sn_2Se_2}$ has $a = 5.5635$ Å and $\alpha = 58.3°$. Both $\mathbf{Co_3Sn_2S_2}$ and $\mathbf{Co_3Sn_2Se_2}$ are centrosymmetric at the Sn site $[0.5, 0.5, 0.5]$ in the Wyckoff position. In contrast, $\mathbf{Co_3Sn_2SeS}$ lacks this symmetry because Se and S atoms are substituted. All structural parameters come from experimental data [61]. Collinear ferromagnetic calculations for all $\mathbf{Co_3Sn_2S_{(2-x)}Se_{(x)}}$ compounds yield spin moment of $1.08\mu_B$ and orbital moment of $-0.02\mu_B$.

4.2 Spin Chiral Interaction

Evaluating magnetic interactions requires self-consistent calculations to obtain energy curves for the homogeneous spin spiral and the noncoplanar schemes. The three distinct spin moment directions of the Co atoms on the kagome lattice are labeled $\vec{\boldsymbol{S}}_i$ and described by:

$$\vec{S}_i = (\sin\phi_i \cos\theta_i; \sin\phi_i \sin\theta_i; \cos\theta_i) \tag{1}$$

For spin spiral case, we change the angle $\phi_i = \phi$ while $\theta_i = \pi/2$ (see Fig.1.b). For the noncoplannar case, we start from the ferromagnetic configuration along x-direction. Here, $\theta_i = \{\pi/2-\theta; \pi/2; \pi/2\}$ and $\phi_i = \{0; \theta/2; -\theta/2\}$ are for azimuthal and polar angles for Co atoms, respectively. Thus, the spin configuration of ferromagnetic state corresponds to $\theta = 0$ and that of noncoplannar case corresponds to $\theta \neq 0$ (see Fig.1.a).

To further probe the role of SOC in $\mathbf{Co_3Sn_2S_{(2-x)}Se_{(x)}}$, we use first-order correction in noncoplanar case embedded in FLEUR code [58, 59]. As a result, the spin-chiral interaction can be expressed as

$$\begin{aligned} E_{SC} &= -\sum_i \kappa_i^{SC} \vec{\boldsymbol{L}}_i^{TO} \cdot \vec{\boldsymbol{S}}_i \\ &= -\sum_{i(jk)} \kappa_{ijk}^{SC} [\vec{\boldsymbol{S}}_i (\vec{\boldsymbol{S}}_j \times \vec{\boldsymbol{S}}_k)] (\vec{\boldsymbol{\tau}}_{ijk} \cdot \vec{\boldsymbol{S}}_i) \end{aligned} \tag{2}$$

The magnetic structure defined in Eq.(1) produces a nonzero scalar chiral product $\chi_{ijk} = \sin^2(\theta)$. This aligns the topological-orbital moment $\vec{\boldsymbol{L}}_i^{TO}$ with the normal surface of the triangle spin lattice τ_{ijk} of the Kagome net. Since the normal surface vector of the kagome net points along the z-direction, the SOC projection is also taken along z-direction. The spin-chiral interaction strength is given by $\kappa_{ijk}^{SC} = \chi_{ijk}^{SO} \kappa_{ijk}^{TO}$, where the scalar quantities originate from the topological orbital moment L_i^{TO} of each magnetic Co atom [24]. The energy function described SCI as the function of θ can be written as $E_{SCI} = -\kappa^{SC} \sin^3\theta$.

To understand the behavior of E_{MCA} in three-dimensional spheres, we calculate the energy difference between different angles of the magnetization axis in this system, which can be expressed by the following formula[45]:

$$\begin{aligned} E_{\text{total}} = K_0 &+ K_1 \alpha_3^2 \\ &+ K_2 \left(\alpha_1^6 - 15\alpha_1^4\alpha_2^2 + 15\alpha_1^2\alpha_2^4 - \alpha_2^6\right) \\ &+ K_3 \alpha_3 \left(\alpha_1^3 - 3\alpha_1\alpha_2^2\right) \end{aligned} \tag{3}$$

where α_1, α_2 and α_3 are the direction cosines of the spontaneous magnetization. We then plot magnetocrystalline anisotropic surface based on the obtained energy values.

Under the projection along z-direction, the magneticrystalline anisotropic energy can be written as $E_{MAE} = -K_1 \left[1 - \cos^2(\theta)\right]$, where K_1 is the dominant term in MAE as indicated in the main text. In addition, since only Co_1 has out-of-plane components $S_1 = \left(0, 0, \cos\left(\frac{\pi}{2} - \theta\right)\right)$, we simplify the contribution of K_1 of E_{MAE} is only one-third compared to the strength of MAE. Similarly, DM energy variation along z-direction can be described as $E_{DMI} = \sum_{ij} D_{ij} S_i \times S_j = -D\sin(\theta)$. Further details of the derivation of these energy functions can be found in S1 section from SI. The fitting energy functions for our

shandite system under the effect of SOC in noncoplanar spin configurations can be written as follows:

$$\begin{aligned} \Delta E_{SOC} &= E_{SCI} + E_{MAE} + E_{DMI} \\ &= \kappa^{SC} \sin^3\theta - K_1 \sin^2\theta - D \sin\theta \end{aligned} \tag{4}$$

References

[1] Burkov, A. Weyl metals. *Annual Review of Condensed Matter Physics* **9**, 359–378 (2018).

[2] Bernevig, B. A., Felser, C. & Beidenkopf, H. Progress and prospects in magnetic topological materials. *Nature* **603**, 41–51 (2022).

[3] Yan, B. & Felser, C. Topological materials: Weyl semimetals. *Annual Review of Condensed Matter Physics* **8**, 337–354 (2017).

[4] Yu, J. *et al.* Quantum geometry in quantum materials. *npj Quantum Materials* **10**, 101 (2025).

[5] Ohta, T., Bostwick, A., Seyller, T., Horn, K. & Rotenberg, E. Controlling the electronic structure of bilayer graphene. *Science* **313**, 951–954 (2006).

[6] Cao, Y. *et al.* Unconventional superconductivity in magic-angle graphene superlattices. *Nature* **556**, 43–50 (2018).

[7] Andrei, E. Y. & MacDonald, A. H. Graphene bilayers with a twist. *Nature Materials* **19**, 1265–1275 (2020).

[8] Gooth, J. *et al.* Axionic charge-density wave in the weyl semimetal (tase4)2i. *Nature* **575**, 315–319 (2019).

[9] Shi, W. *et al.* A charge-density-wave topological semimetal. *Nature Physics* **17**, 381–387 (2021).

[10] Hanke, J.-P., Freimuth, F., Niu, C., Blügel, S. & Mokrousov, Y. Mixed weyl semimetals and low-dissipation magnetization control in insulators by spin–orbit torques. *Nature Communications* **8**, 1479 (2017).

[11] Niu, C. *et al.* Mixed topological semimetals driven by orbital complexity in two-dimensional ferromagnets. *Nature Communications* **10**, 3179 (2019).

[12] Dzyaloshinsky, I. A thermodynamic theory of ‚Äúweak‚Äù ferromagnetism of antiferromagnetics. *Journal of Physics and Chemistry of Solids* **4**, 241–255 (1958).

[13] Moriya, T. Anisotropic superexchange interaction and weak ferromagnetism. *Phys. Rev.* **120**, 91–98 (1960).

[14] Freimuth, F., Bamler, R., Mokrousov, Y. & Rosch, A. Phase-space berry phases in chiral magnets: Dzyaloshinskii-moriya interaction and the charge of skyrmions. *arXiv preprint arXiv:1307.8085* (2013).

[15] Bogdanov, A. N. & Yablonskii, D. Thermodynamically stable "vortices" in magnetically ordered crystals. the mixed state of magnets. *Zh. Eksp. Teor. Fiz* **95**, 178 (1989).

[16] Mühlbauer, S. *et al.* Skyrmion lattice in a chiral magnet. *Science* **323**, 915–919 (2009).

[17] Parkin, S. S. P., Hayashi, M. & Thomas, L. Magnetic domain-wall racetrack memory. *Science* **320**, 190–194 (2008).

[18] Tomasello, R. *et al.* A strategy for the design of skyrmion racetrack memories. *Scientific Reports* **4**, 6784 (2014).

[19] Bruno, P., Dugaev, V. K. & Taillefumier, M. Topological hall effect and berry phase in magnetic nanostructures. *Phys. Rev. Lett.* **93**, 096806 (2004).

[20] Kimbell, G., Kim, C., Wu, W., Cuoco, M. & Robinson, J. W. A. Challenges in identifying chiral spin textures via the topological hall effect. *Communications Materials* **3**, 19 (2022).

[21] Heide, M., Bihlmayer, G. & Blügel, S. Dzyaloshinskii-moriya interaction accounting for the orientation of magnetic domains in ultrathin films: Fe/w (110). *Physical Review B—Condensed Matter and Materials Physics* **78**, 140403 (2008).

[22] Wang, X., Yuan, H. & Wang, X. A theory on skyrmion size. *Communications Physics* **1**, 31 (2018).

[23] Jiang, H., Zhang, J. & Zhou, Y. Higher-order magnetic interactions and topological textures in fe 3 gete 2: Influence of spin-orbit coupling. *Physical Review B* **111**, 214429 (2025).

[24] Grytsiuk, S. *et al.* Topological–chiral magnetic interactions driven by emergent orbital magnetism. *Nature communications* **11**, 511 (2020).

[25] Singh, C. *et al.* Higher order exchange driven noncoplanar magnetic state and large anomalous hall effects in electron doped kagome magnet mn3sn. *npj Quantum Materials* **9**, 43 (2024).

[26] Kolincio, K. K. *et al.* Kagome lattice promotes chiral spin fluctuations. *Physical Review Letters* **130**, 136701 (2023).

[27] Zhang, W., Zhou, J. & Cheng, S. Valley transport in breathing kagome lattices with chiral spin textures. *Physical Review B* **111**, 165307 (2025).

[28] van Walsem, E., Duine, R. A. & Guimarães, M. H. Layer effects on the magnetic textures in magnets with local inversion asymmetry. *Physical Review B* **102**, 174403 (2020).

[29] Liu, E. *et al.* Giant anomalous hall effect in a ferromagnetic kagome-lattice semimetal. *Nature physics* **14**, 1125–1131 (2018).

[30] Mitscherling, J. Longitudinal and anomalous hall conductivity of a general two-band model. *Physical Review B* **102**, 165151 (2020).

[31] Sakai, Y., Kamihara, Y. & Matoba, M. Magnetic properties of shandite-type co3sn2s2-xsex. *physica status solidi c* **10**, 1130–1131 (2013).

[32] Shin, D.-H., Jun, J.-H., Lee, S.-E. & Jung, M.-H. Degenerate magnetic ground state and metastable state on trihexagonal co-sublattices in co3sn2 (s, se) 2 single crystals. *arXiv preprint arXiv:2105.03892* (2021).

[33] Barua, A. *et al.* Competing and anisotropic exchange interactions in the kagome lattice ferromagnet co3sn2s2. *physica status solidi (b)* 2400520 (2025).

[34] Guguchia, Z. *et al.* Tunable anomalous hall conductivity through volume-wise magnetic competition in a topological kagome magnet. *Nature communications* **11**, 559 (2020).

[35] Wu, H. *et al.* Observation of skyrmion-like magnetism in magnetic weyl semimetal co3sn2s2. *Materials Today Physics* **12**, 100189 (2020).

[36] Kassem, M. A., Tabata, Y., Waki, T. & Nakamura, H. Low-field anomalous magnetic phase in the kagome-lattice shandite c o 3 s n 2 s 2. *Physical Review B* **96**, 014429 (2017).

[37] Fujiwara, K. *et al.* Giant antisymmetric magnetoresistance arising across optically controlled domain walls in the magnetic weyl semimetal co3sn2s2. *Communications*

Materials **5**, 239 (2024).
[38] Sugawara, A. *et al.* Magnetic domain structure within half-metallic ferromagnetic kagome compound c o 3 s n 2 s 2. *Physical Review Materials* **3**, 104421 (2019).
[39] Pate, S. *et al.* Anomalies in the electromagnetic response and peculiarities of the domain structure in the magnetic weyl semimetal co 3 sn 2 s 2. *Physical Review B* **111**, 054439 (2025).
[40] Yin, J.-X. *et al.* Negative flat band magnetism in a spin–orbit-coupled correlated kagome magnet. *Nature Physics* **15**, 443–448 (2019).
[41] Nag, A. *et al.* Correlation driven near-flat band stoner excitations in a kagome magnet. *Nature Communications* **13**, 7317 (2022).
[42] Xu, Y. *et al.* Electronic correlations and flattened band in magnetic weyl semimetal candidate co3sn2s2. *Nature communications* **11**, 3985 (2020).
[43] Heide, M., Bihlmayer, G. & Blügel, S. Describing dzyaloshinskii–moriya spirals from first principles. *Physica B: Condensed Matter* **404**, 2678–2683 (2009).
[44] Kuz'Min, M., Skokov, K., Diop, L., Radulov, I. & Gutfleisch, O. Exchange stiffness of ferromagnets. *The European Physical Journal Plus* **135**, 1–8 (2020).
[45] Döring, W. Die richtungsabhängigkeit der kristallenergie. *Annalen der Physik* **456**, 102–109 (1957).
[46] Shen, J. *et al.* On the anisotropies of magnetization and electronic transport of magnetic weyl semimetal co3sn2s2. *Applied Physics Letters* **115** (2019).
[47] Lee, C. *et al.* Observation of a phase transition within the domain walls of ferromagnetic co3sn2s2. *Nature communications* **13**, 3000 (2022).
[48] Shiogai, J. *et al.* Electrical detection of domain evolution in magnetic weyl semimetal co 3 sn 2 s 2 submicrometer-wide wire devices. *Physical Review Materials* **6**, 114203 (2022).
[49] Xu, Q. *et al.* Topological surface fermi arcs in the magnetic weyl semimetal co 3 sn 2 s 2. *Physical Review B* **97**, 235416 (2018).
[50] Mazzola, F. *et al.* Signatures of a surface spin–orbital chiral metal. *Nature* **626**, 752–758 (2024).
[51] Rimmler, B. H., Pal, B. & Parkin, S. S. Non-collinear antiferromagnetic spintronics. *Nature Reviews Materials* **10**, 109–127 (2025).
[52] Zyuzin, A. A. & Tiwari, R. P. Intrinsic anomalous hall effect in type-ii weyl semimetals. *JETP letters* **103**, 717–722 (2016).
[53] Burkov, A. & Balents, L. Weyl semimetal in a topological insulator multilayer. *Physical review letters* **107**, 127205 (2011).
[54] Das, K. & Agarwal, A. Linear magnetochiral transport in tilted type-i and type-ii weyl semimetals. *Physical Review B* **99**, 085405 (2019).
[55] Wei, X.-P., Yang, N., Shen, J. & Tao, X. Ferromagnetic weyl semimetals and quantum anomalous hall effect in 2d half-metallic mn2nt2. *Physica E: Low-dimensional Systems and Nanostructures* **140**, 115164 (2022).
[56] Zhang, C.-L. *et al.* Magnetic-tunnelling-induced weyl node annihilation in tap. *Nature Physics* **13**, 979–986 (2017).
[57] Pate, S. *et al.* Anomalies in the electromagnetic response and peculiarities of the domain structure in the magnetic weyl semimetal co 3 sn 2 s 2. *Physical Review B* **111**, 054439 (2025).

[58] The FLEUR project. https://www.flapw.de/.
[59] Wimmer, E., Krakauer, H., Weinert, M. & Freeman, A. J. Full-potential self-consistent linearized-augmented-plane-wave method for calculating the electronic structure of molecules and surfaces: o_2 molecule. *Phys. Rev. B* **24**, 864–875 (1981).
[60] Perdew, J. P., Burke, K. & Ernzerhof, M. Generalized gradient approximation made simple. *Physical review letters* **77**, 3865 (1996).
[61] Weihrich, R. *et al.* Tuneable anisotropy and magnetism in sn 2 co 3 s 2- x se x–probed by 119 sn mößbauer spectroscopy and dft studies. *Dalton Transactions* **44**, 15855–15864 (2015).

Data availability. All data needed to evaluate the conclusions in the paper are available within the article. All raw data generated during the current study are available from the corresponding author upon request.

Code availability. The codes used for the DFT calculations in this study are available from the corresponding authors upon request.

Acknowledgements. This work at USF was based upon work supported by the Air Force Office of Scientific Research under award number FA9550−23−1−0132 and US Department of Energy (DOE) under Grant No. DE−FG0207ER46438. J.G. and D.K.L. acknowledges support from the Max Planck Society through the Max Planck Partner Group Programme and CS−CSA−2024−106 from Research Corporation for Science Advancement. Y.M. acknowledges support by the Deutsche Forschungsgemeinschaft (DFG) in the framework of TRR 288/2 − 422213477 (Project B06) and by the Jülich Supercomputing Centre (jiff40).

Author contribution. D.K.L. and J.G. proposed and designed the research. D.K.L. contributed to the DFT calculations. J.G., T.S. and Y.M. proposed spin-chiral interaction. D.K.L. and B.K. obtain band structure. L.D.K., E.K. and G.P. analyzed magnetic interaction. D.K.L, E.K. and J.G. analyzed data. D.K.L., E.T. and M.H.P wrote the paper. All authors discussed the results and commented on the manuscript.

Supplementary information. Supplementary information is available in the supplementary information file.

Competing interests. The authors declare no competing interests.

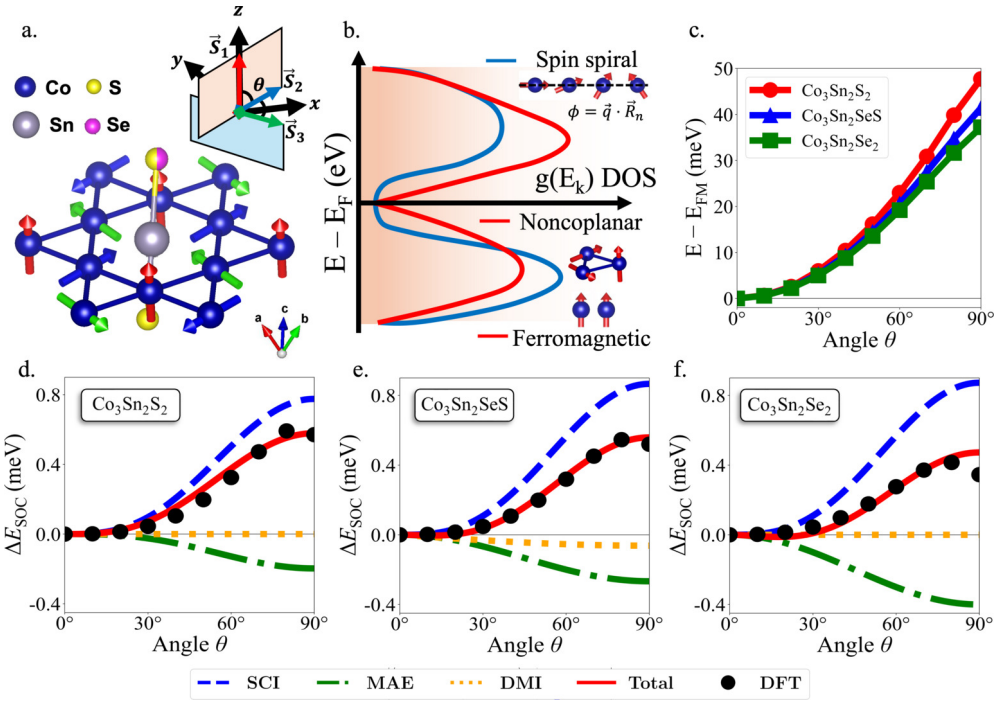

Figure 1 Disentangling energy contribution of noncoplannar spin configuration of Co atoms on Kagome net. (a) Side view of lattice structure of $Co_3Sn_2S_{(2-x)}Se_{(x)}$, where Co, Sn, S, and Se atoms are indicated in blue, gray, yellow, and green, respectively. (b) The kagome lattice formed by the Co atoms shows the noncoplanar magnetic state with a nonzero scalar chiral product. The inset displays the magnetic directions of the Co_1, Co_2, and Co_3 atoms in the Cartesian coordinate system, labeled with red, blue, and green arrows, respectively. (c) The energy dispersion relation of all shandite compounds with the noncoplanar spin orientations. (d–f) The comparison of spin-orbit-induced energy in (d) $Co_3Sn_2S_2$, (e) Co_3Sn_2SeS, and (f) $Co_3Sn_2Se_2$ between the DFT calculations (circles) and the spin-orbit contribution terms (lines), where the antisymmetric exchange (DMI) is shown as a green dash–dot line, while the spin-chiral interaction (SCI) is shown as a blue dashed line.

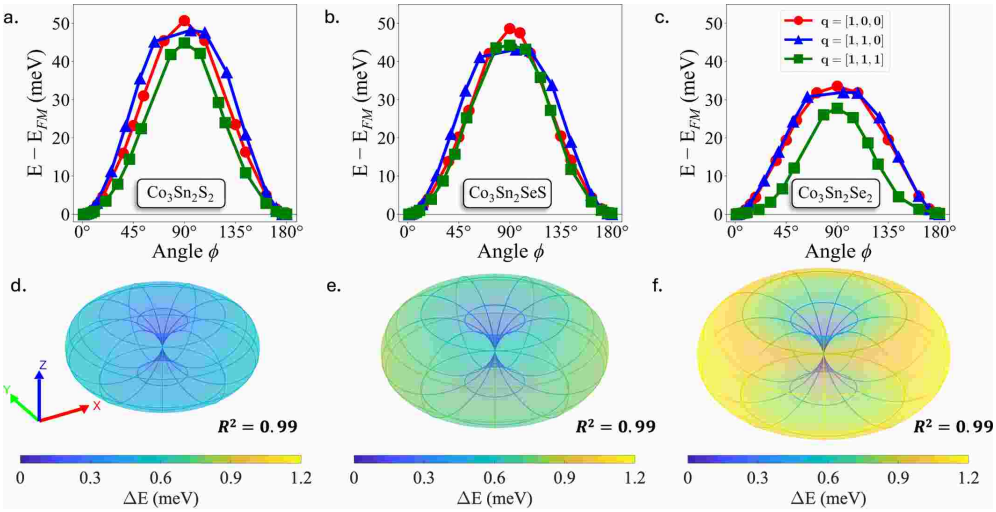

Figure 2 The dispersion relation in flat spin spirals and magnetocrystalline anisotropy surface of all shandite compounds. (a-c) Energy dispersion of spin spirals along [1,0,0] [1,1,0] and [1,1,1] directions (without SOC consideration), for (a) $Co_3Sn_2S_2$, (b) Co_3Sn_2SeS, and (c) $Co_3Sn_2Se_2$. (d-f) Three-dimensional magnetocrystalline anisotropy surfaces reflect the magnetocrystalline anisotropy energy of (d) $Co_3Sn_2S_2$, (e) Co_3Sn_2SeS, and (f) $Co_3Sn_2Se_2$.

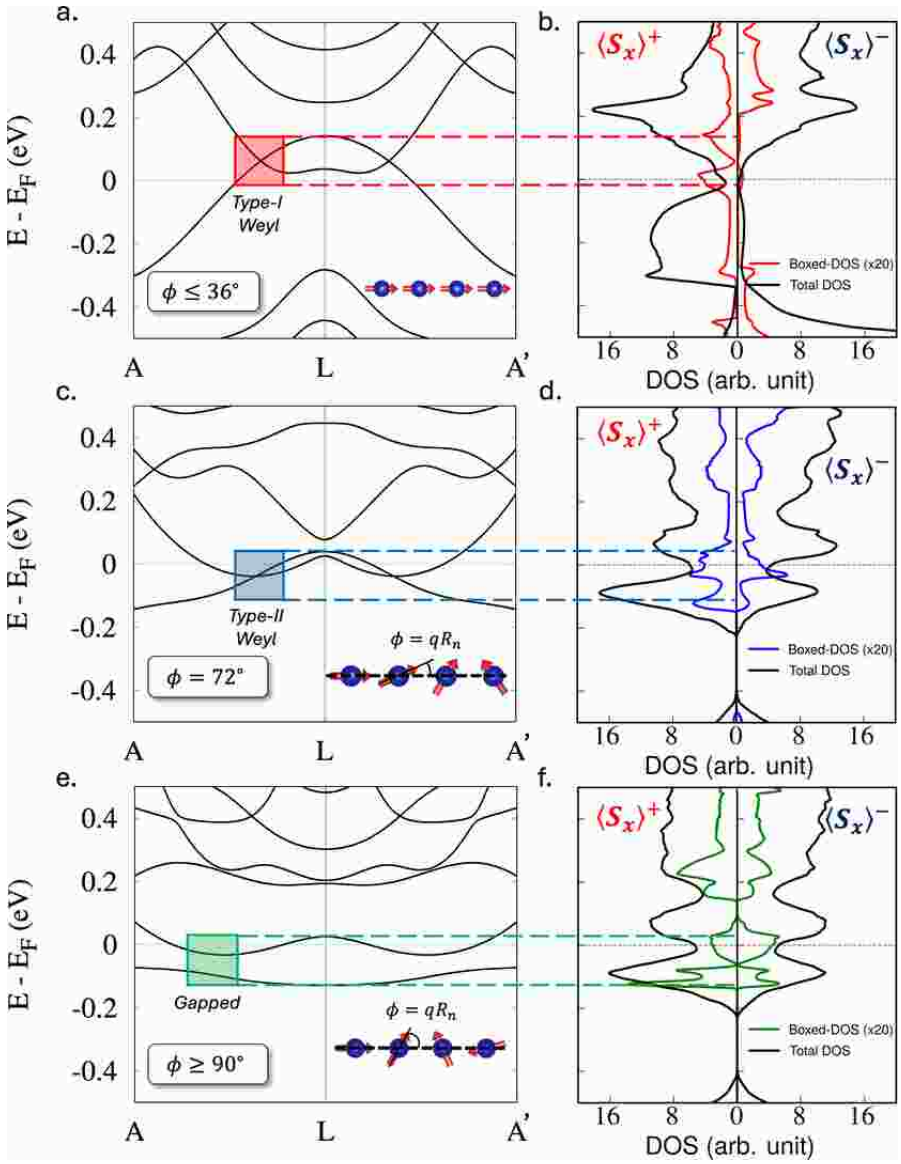

Figure 3 Electronic band structures and density of states (DOS) of $Co_3Sn_2S_2$. Band structure and DOS are illustrated for $\phi = 0°$ in (a-b), $\phi = 72°$ in (c-d), and $\phi = 108°$ in (e-f), respectively. The spin projection in DOS is along the x-direction.

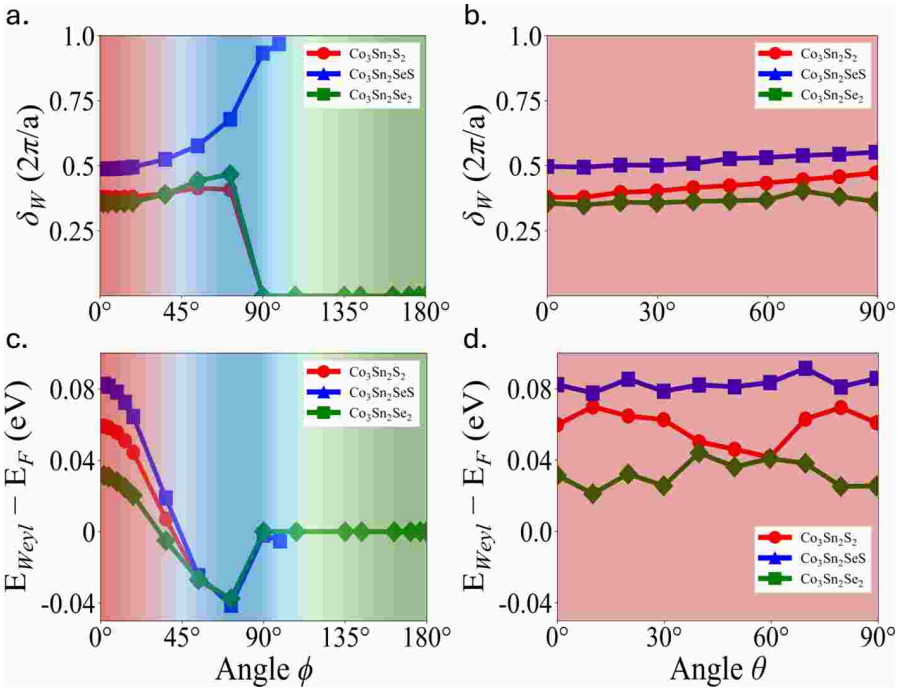

Figure 4 Topological phase transitions of $Co_3Sn_2S_{2-x}Se_{(x)}$. Topological phase transitions of $Co_3Sn_2S_2$, Co_3Sn_2SeS, and $Co_3Sn_2Se_2$ are in red, blue and green lines, respectively. (a,b) Distance between two Weyl crossings is plotted as a function of the spin spiral angle ϕ (along the direction q = [1, 0, 0]) and the noncoplanar angle θ. (c,d) Position of the Weyl pairs with respect to the Fermi energy as a function of both the mentioned angles.

Supplementary Files

This is a list of supplementary files associated with this preprint. Click to download.

- CPSI.pdf
- Table1.docx